The Effect of Internal Wave-Related Features on Synthetic Aperture Sonar

Roy Edgar Hansen, *Member, IEEE*, Anthony P. Lyons, *Member, IEEE*, Torstein Olsmo Sæbø, *Senior Member, IEEE*, Hayden John Callow, *Member, IEEE*, and Daniel A. Cook, *Senior Member, IEEE*

Abstract—In October 2012, the Centre for Maritime Research and Experimentation (CMRE, La Spezia, Italy) conducted trials from the NATO research vessel (RV) *Alliance*, off Elba Island, Italy. During this trial, data were collected by the Norwegian Defence Research Establishment (FFI, Kjeller, Norway) using a HUGIN autonomous underwater vehicle (AUV) with interferometric synthetic aperture sonar (SAS) in repeated passes. Large linear structures (tens of meters by several meters) observed in both the SAS images and SAS bathymetry during the initial pass were absent in data taken on a repeated pass the following day. We suggest that these phenomena were not true seafloor features, but were caused by features in the water column, known as boluses, which can form after breaking internal wave events. The changes observed in acoustical intensity and phase appear to be caused by the interaction of the acoustical field with the lower average sound-speed structure of the bolus, constructing features in both SAS imagery and SAS bathymetry that looked like seabed topography. In this paper, we present examples and give an interpretation of the results based on an acoustical ray model. We discuss different techniques for recognizing these phenomena: repeat pass imaging and interferometry, multilook and multiaperture processing, and moving target analysis.

Index Terms—Internal waves, refraction effects, synthetic aperture sonar.

I. INTRODUCTION

SYNTHETIC aperture sonar (SAS) is a major tool for seabed imaging and mapping, providing very fine resolution and high image quality. Although SAS technology today is well known and has a long history, it is only within the last decade that it has matured substantially and become more readily available [1], [2]. As in synthetic aperture radar (SAR)

[3], [4], SAS is a technique that produces images that are well suited for estimating coherent or noncoherent changes over repeated passes, a technique known as change detection [5].

All types of sonar are affected by the ocean environment, and the vertical sound-speed profile is particularly influential [6, Ch. 2]. In SAS, the two most dominant effects caused by incorrect knowledge of the sound speed are defocusing, especially for widebeam systems [7], [8], and bias in the seabed depth estimation using interferometry. The latter is also a common issue for multibeam echosounders [6, Ch. 8.3]. Strong variability in the ocean sound-speed structure induced by internal waves or turbulence also exists, and can limit the temporal and spatial coherence of acoustical signals in sonar [9]. Experiments have shown that this problem in many cases is not large enough to be restrictive in SAS [10], [11]. At present, most SAS processing algorithms also use data-driven navigation (known as micronavigation) [12] to achieve the required position accuracy for successful SAS imaging. Micronavigation will inherently reduce the effect of the variability in the water column in SAS [13].

In October 2012, the Centre for Maritime Research and Experimentation (CMRE, La Spezia, Italy) conducted the 2012 Autonomous Reactive Intelligence Sea Experiment (ARISE'12) trial from the NATO research vessel (RV) *Alliance*, off Elba Island, Italy. During this trial, change detection data were collected by the Norwegian Defence Research Establishment (FFI, Kjeller, Norway) using a HUGIN autonomous underwater vehicle (AUV) with interferometric SAS (see Fig. 1). Large linear structures (tens of meters by several meters) in the SAS images and in the SAS bathymetry apparently disappeared or changed in repeated passes with 28-h time separation. These changes were present near a depth where a strong density and sound-speed step intersected the sloping seafloor. The weather was calm and the sea state was low during the trial period. Similar features were observed multiple times over several days in the same area.

We suggest that these anomalies in the SAS images and the SAS bathymetry estimates were not caused by changes in the seafloor, but by water column features known as boluses which result from breaking internal waves [14]–[17]. Internal wave boluses are formed after an internal wave breaking event captures colder water within a small area surrounded by warmer water. These internal wave boluses then move slowly up-slope along the seabed. The changes observed in acoustical intensity and phase can be described by refraction as propagating acoustical waves interact with the variation in sound speed caused by the bolus. Our interpretation of this phenomenon is based on a ray model that describes the variation in backscattered intensity
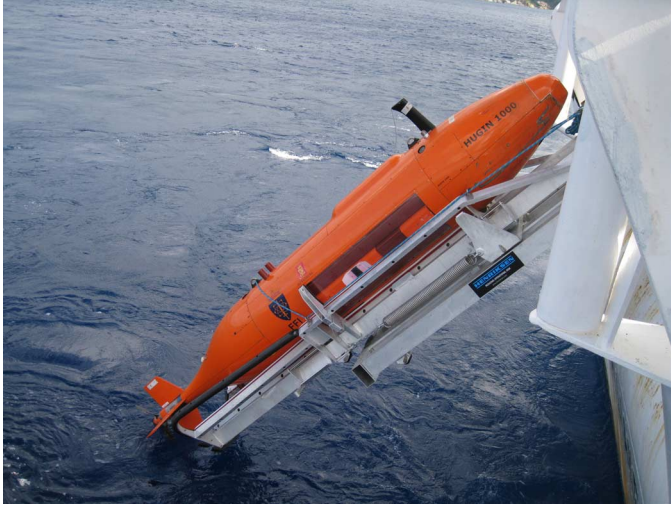
Fig. 1. The HUGIN AUV with the HISAS wideband interferometric SAS during launch from NATO *RV Alliance* in October 2012.

TABLE I
SYSTEM SPECIFICATIONS DURING THE DATA ACQUISITION

Center frequency	100 kHz
Wavelength	1.5 cm
Bandwidth	30 kHz
Interferometric baseline	30 cm
Along-track resolution	< 4 cm
Cross-track resolution	< 4 cm
Maximum range @ 2 m/s	200 m

from the seabed as a focusing of sound by the bolus, and describes the error in the SAS bathymetry by the refractive effect caused by the bolus. A similar effect has been documented in airborne SAR [18]–[20].

In Section II, we show SAS images and bathymetries of the phenomena. In Section III, we apply a simple ray acoustical model to describe the refractive effects from such anomalies in the water column. Section IV lists potential techniques to establish if a feature in a SAS image is a true feature on the seabed or an artificial feature caused by refractive effects. Finally, we summarize the findings in Section V.

II. ILLUSTRATION OF THE PHENOMENA

The HISAS 1030 is a programmable wideband interferometric SAS suitable for high-resolution imaging and mapping of the seabed [8], [21]. The sensor is operated from HUGIN AUVs at a typical vehicle altitude above the seabed of 10–20 m. All data examples in this paper are collected with this sensor. Table I summarizes the key system specifications during the experiment. The images are created using the backprojection algorithm in ground coordinates, after micronavigation is applied [8].

Fig. 2(a) shows a SAS image covering 60×60 m^2 of the seabed at approximately 46-m water depth. The theoretical along-track and cross-track resolution in the image is 3.7×3.3 cm^2. Fig. 2(b) shows a SAS image made of the same scene 28 h later. The yellow circles in the two images indicate small rocks that are present in both images. The images are

coregistered to subpixel accuracy [22], [23, Ch. 5.3]. The large diagonal feature in the top portion of the left panel is entirely consistent with intensity variations caused by slope changes from a ridge of sand. The apparent ridge is absent in the image collected 28 h later. The sea state during the period was low and so sediment transport could not remove such a large feature.

Fig. 3 shows the intensity profile slice from both images in Fig. 2 at along-track position $x = 47$ m. The profiles are calculated by averaging over 2 m along track and applying a 26-cm boxcar averaging cross track. The intensity variation caused by the phenomenon is 6 dB stronger in the highlight region and 10 dB weaker in the shadow region. These are strong variations and would be easily seen as an anomaly in change detection.

The sensor used in the experiment contains two vertically offset receiver arrays allowing for single-pass SAS interferometry. Fig. 4 shows the estimate of the seabed depth from the interferometric processing in the presence of the suspected internal wave bolus shown in Fig. 2(a). The average slope of the seabed is removed (the data are detrended). We have performed the interferometric processing with the weighted multiband split-spectrum algorithm and an 18×18-cm^2 interferogram estimation window [24]. The map shows a ridge shape with a seabed depth profile that would be expected from the variation in the backscattered intensity shown in the SAS image. The interferometric coherence [25, Ch. 4.3] is high, indicating that the interferometric image pairs are accurately coregistered and that there are valid backscattered signals in the full scene including the apparent shadow region. In the repeated pass seabed depth estimate, there is no visible sign of the feature (similar to the repeated pass intensity image shown in Fig. 2).

Fig. 5 shows profiles of estimated seabed depth from SAS bathymetry taken on both days at an along-track position $x = 47$ m (the same position as the profiles displayed in Fig. 3). In the profile with the suspected bolus present, the estimated height of the apparent ridge is seen to be approximately 20–30 cm. We also see that the apparent depth slope after the internal wave feature is different between the two days. This can be explained by small changes in the thermocline between the passes, and ignoring the refraction effect in the interferometric processing. Refraction effects are discussed in detail in Section III.

III. ACOUSTICAL REFRACTIVE MODEL

Fig. 6 shows the average temperature profile, density profile, and sound-speed profile based on conductivity–temperature–depth (CTD) measurements taken October 20, 2012, in the trial area. There is a strong step change in both the density and the sound speed from around 40-m depth to 60-m depth, caused by a seasonal thermocline which is common in the Mediterranean in the late summer and early fall. This large gradient creates conditions suitable for propagating internal waves and consequently refractive effects on acoustical wave propagation. For the data example in Section II, the sloping seabed intersects with the density step similarly as in [17], indicating the possibility of existence of internal wave boluses.

To understand how a water column effect can cause features similar to our observations, we develop a simple ray model. We follow [15] and assume a simplified parabola-shaped wave feature of cold dense water with sound speed c_1 and density ρ_1
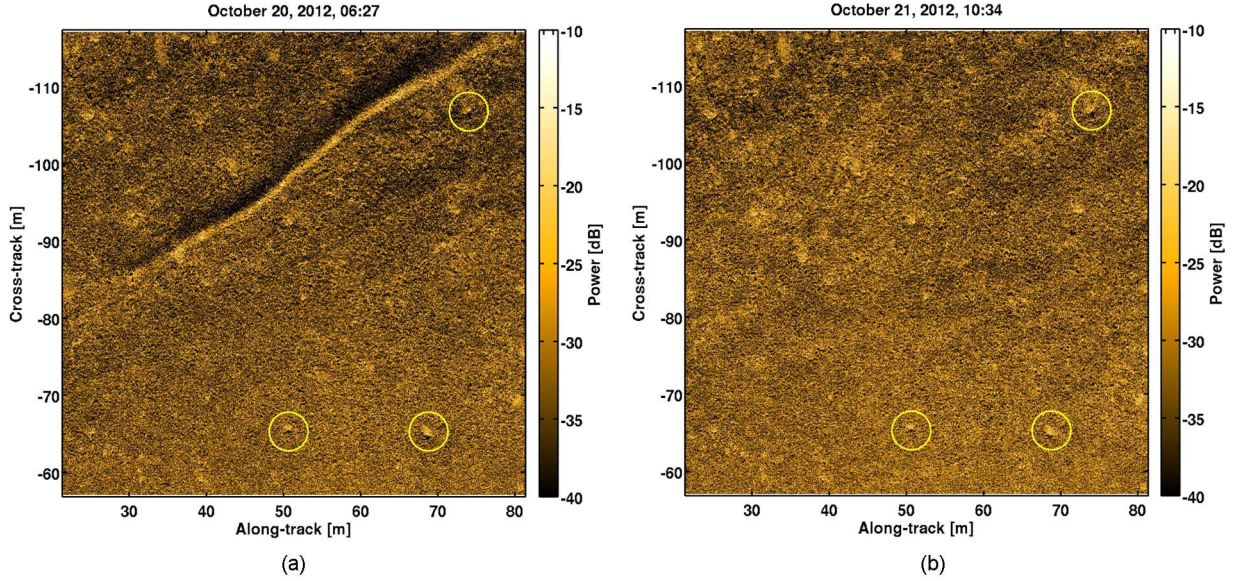
Fig. 2. SAS images of the same scene taken on October 20 and 21, 2012, 28 h apart. Panel (a) is the earliest. The yellow circles highlight small rocks in the scene indicating that the images are accurately coregistrated.
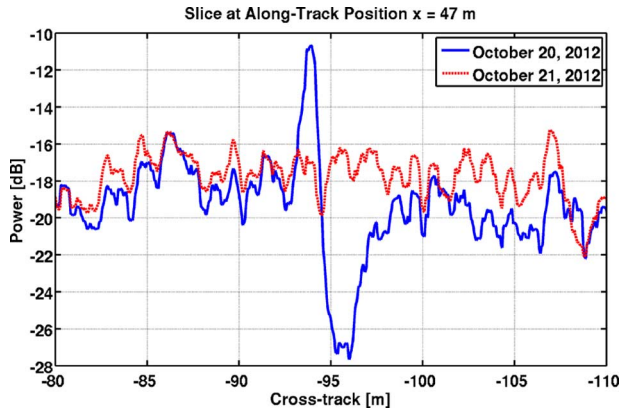

Fig. 3. Slice through the images shown in Fig. 2 at $x = 47$ m.

lying on the seabed surrounded by warmer lighter water with sound speed c_0 and density ρ_0. This is illustrated in Fig. 7. Following [26, Ch. 3.1], the reflection coefficient for normal incidence is

$$V = \frac{m - n}{m + n}, \qquad \text{where } m = \frac{\rho_1}{\rho_0} \quad \text{and} \quad n = \frac{c_1}{c_0}. \quad (1)$$

For the case shown in Fig. 6, we have $c_0 = 1530$ m/s, $c_1 = 1510$ m/s, $\rho_0 = 1028.5$ kg/m^3, and $\rho_1 = 1027$ kg/m^3. This gives a reflection coefficient of $V \approx 0.007$, indicating that backscattering from the internal wave itself is very difficult to detect if not impossible for a side-looking sonar geometry. Echoes from the seabed will also be present at the same slant range as the internal wave, and they will most likely mask the potential echo from the internal wave itself. Note that this is different from the observations documented in [17], where a narrowbeam downward-looking sonar was used.

It is straightforward to apply Snell's law of refraction for each ray at each of the interfaces between cold and warm water. For convex surfaces encapsulating lower sound speeds, incoming
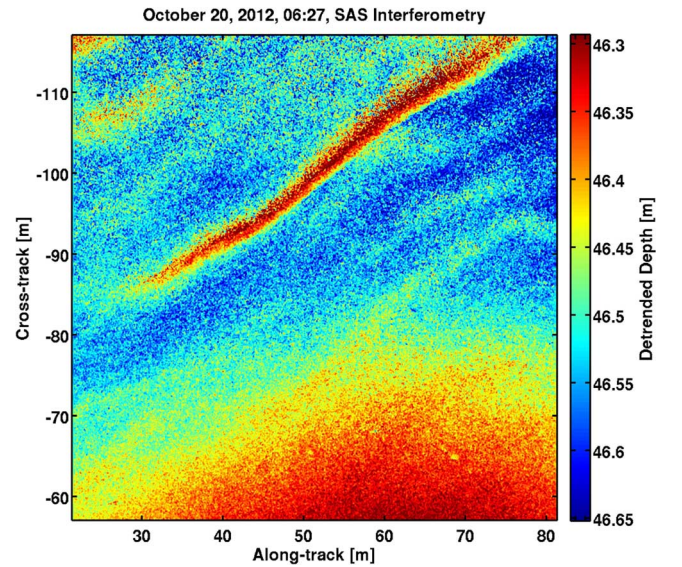

Fig. 4. Seabed depth estimate from SAS interferometry based on the image shown in Fig. 2(a). The average slope has been removed.
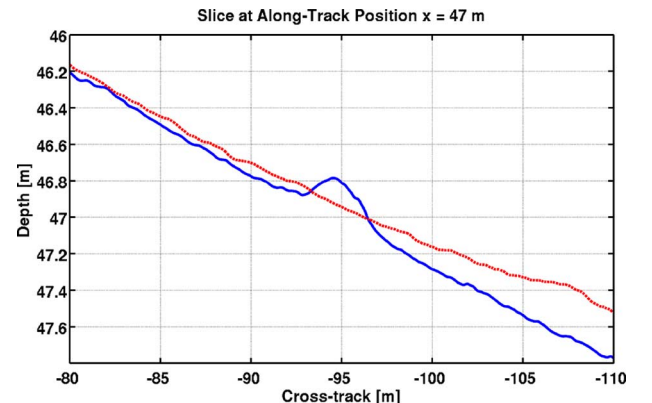

Fig. 5. Slice through the bathymetry shown in Fig. 4 compared with the repeated pass at $x = 47$ m.

horizontal acoustical rays from a source will be refracted toward the seabed. The effect in the image will be a function of
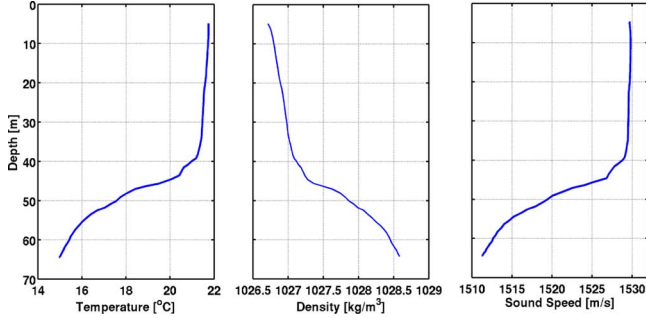
Fig. 6. Temperature, density, and sound-speed profile taken during the experiment.
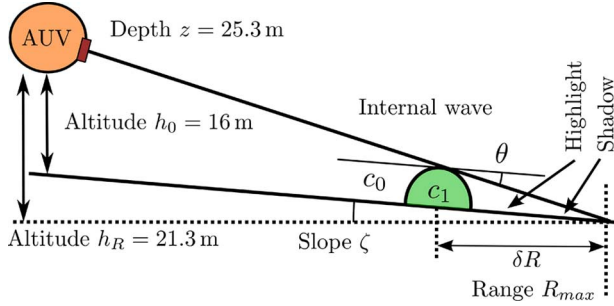

Fig. 7. Vertical geometry of the imaging through an internal wave bolus on a sloping seabed.
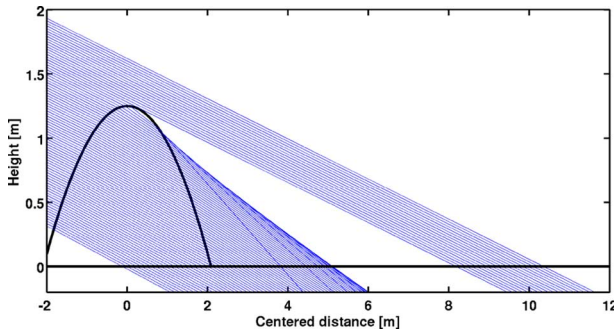

Fig. 8. Interaction of acoustical rays with a parabola containing lower sound speed. Note that the aspect ratio in the plot is not 1:1, causing the rays to appear steeper than what they are.

the sound-speed difference, the exact size and shape of the feature, and geometry. We perform a simple calculation to illustrate the effect. Assume a parabolic shape of height H and width L filled solely with water of sound speed c_1. The vertical shape boundary is described by

$$ z = -\frac{H}{\left(\frac{L}{2}\right)^2}y^2 + H, \quad \frac{dz}{dy} = -\frac{2H}{\left(\frac{L}{2}\right)^2}y \quad (2) $$

where z is the vertical position and y is the horizontal position (cross-track ground range). The derivative and thereby the normal vector is known at each position of the parabola. This can be used in calculating all the angles involved. The individual rays can be traced through the parabola by applying Snell's law.

In [15], the typical shape of the bolus was found to have $H/L \approx 0.3$. Our initial studies [27] suggested that the bolus height (or amplitude) could be around 1.5–3 m. In this simulation, we have chosen $H = 1.25$ m, $L = H/0.3$ to fit the observed shadow length in the data. Fig. 8 shows the results from

our simple ray model. We have chosen incoming rays with an incidence angle of $\theta \approx 16/100 \approx 9°$. This is approximately correct for the data example in Fig. 2 with the corresponding geometry sketched in Fig. 7. Note that the seabed itself is sloping with $\zeta = (h_R - h_0)/R_{\max} \approx 5.3/100 \approx 3°$. The rays that intersect close to the top of the parabola are the rays that refract downward the most. This refraction caused by the bolus gives the lens effect, as described in [20].

From the ray model, it is possible to describe four different effects that may be observed in the SAS images and bathymetry.

1) The ray density on the seabed varies due to the refraction effect. In Fig. 9(a), we show the ray density for the case shown in Fig. 8. The ray density is normalized with respect to the ray density of a homogeneous water column. We see that the ray density increases rapidly and by a factor of 3 until the shadow region appears. This corresponds to approximately 9-dB increase in relative power, but on a very confined small range interval.

2) The increase of grazing angle due to ray steepening will cause a change in scattering strength. There exists various models for roughness scattering from the seabed [28, Ch. 13]. Since these effects are observed close to grazing incidence, a small roughness perturbation approximation model may be used. Fig. 9(b) shows the grazing angle as a function of distance from parabola. Since the refractive effect from the parabola causes rays to cross, there will be multiple grazing angles in a certain range interval. There are, however, very few rays with steep angles due to the small number of rays intersecting with the top part of the parabola. Around the maximum ray density, the grazing angle changes from 9° to around 13°. This corresponds approximately to a difference in backscattering strength of 5 dB for sand seabed types and 3 dB for silt/clay seabed types, when applying the system and the geometry to the APL-UW94 scattering model [29].

3) In the interferometry processing, the seabed topography is estimated from the acoustical ray direction of arrival [25], [30]. The nonlinearity of the rays will cause an error in the SAS interferometric bathymetry. The error may occur even when the interferometric coherence is very high. Refraction-induced errors are a common problem for other bathymetric sensors such as multibeam echosounders [6, Ch. 8.3]. Fig. 9(c) shows the depth error caused by ray nonlinearity for the model case in Fig. 8. As with the grazing angle, there are two conflicting depths for certain distances from the parabola. The largest depth errors (around 0.8-m value) are caused by very few rays, and may not be observable. The depth error around the maximum ray density, which corresponds to the peak in signal intensity, is around 0.3 m.

4) The lowered sound speed c_1 within the parabola will cause a displacement error in the SAS image. The rays that propagate through the parabola will be slowed down slightly such that the texture and speckle in the SAS image behind the parabola will be displaced. This effect will be largest for the rays that intersect the parabola close to the seabed and thereby refract the least. To get a rough estimate of the effect, we assume a ray that intersects the parabola at
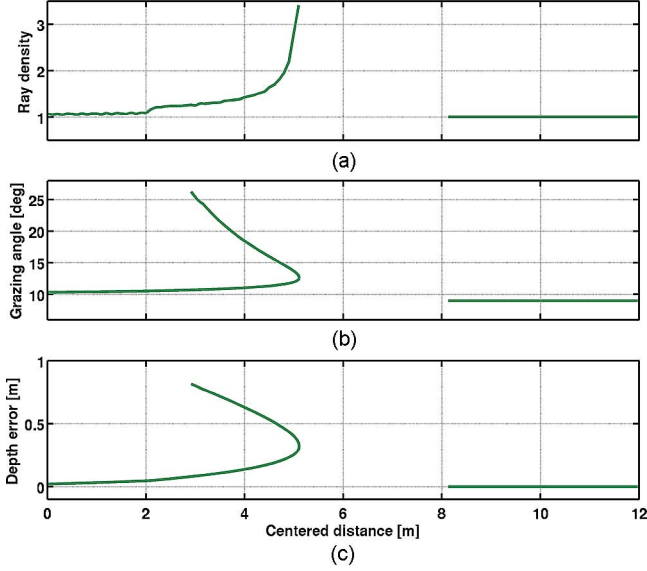
Fig. 9. (a) Ray density, (b) grazing angle, and (c) refraction-induced interferometric depth error for the acoustical rays interacting with the parabola in Fig. 8.
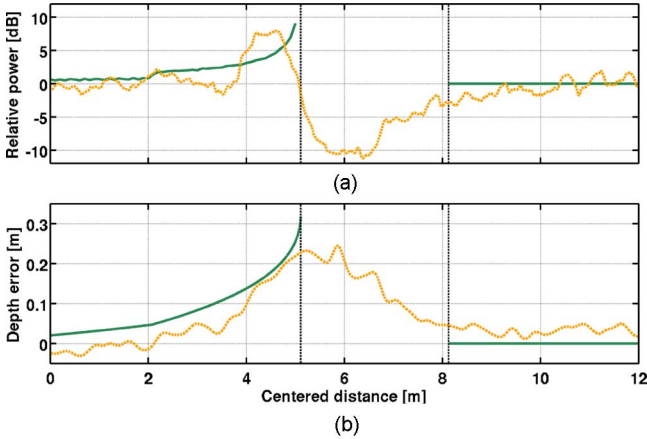
Fig. 10. (a) Modeled signal power (green) compared with measured signal difference. (b) Modeled depth error caused by refraction compared with detrended measured depth.

the half-height of the parabola $H/2$. The approximate horizontal distance through the parabola becomes $\delta L \approx 3.5$ m, giving a displacement error

$$\delta r \approx \delta L(1 - c_1/c_0) \approx 4.5 \text{ cm}. \qquad (3)$$

Note that the ray refraction will also cause displacement in the image, but not as much as that due to lowered sound speed.

These four effects may be used for detecting internal wave boluses in SAS data, and they may also be used to invert for internal wave parameters. There are three noticable effects that will affect the measurements: In our simulated scenario, we use a perfect parabola-shaped bolus. In reality, the shape may be different, and mixing of the water outside and inside the parabola may occur. The second effect lies in the horizontal plane. SAS imaging uses the angular spread over multiple pings to obtain finer along-track resolution. Hence, a bolus will be sampled at different horizontal look angles in one SAS image. Acoustical

waves that propagate through the internal wave boluses may also be refracted horizontally. Finally, the geometry will affect the measurements. A nonplanar seabed topography will cause the internal wave bolus to change direction, shape, and speed, and the SAS data collection will be from an ensemble of geometries, as described by the model.

Due to the sum of all these effects, measurements are expected to contain less extreme boundaries and peak values: in the shadow region, there will still be some signal; the peak depth error will be less than the modeled; the peak signal strength will be less than the modeled; and the far end transition between shadow and normal backscatter behind the affected area will be softened (around centered distance of 9 m in Fig. 8).

Fig. 10(a) shows the measured intensity difference between the two passes shown in Fig. 3 compared with the modeled ray density. The model results are positioned such that the shadow part fits the measurements. Fig. 10(b) shows the detrended SAS bathymetry from Fig. 5 compared with the modeled refraction-induced depth error. The vertical bars indicate the boundaries of the modeled region where ray theory would give no intensity. We have removed the rays that are steeper than the angle at the maximum ray density (the turning point in Fig. 9). There is nonzero energy in the shadow region as well as valid bathymetry estimates, likely due to the effects discussed above.

IV. RECOGNITION OF INTERNAL WAVE PHENOMENA

As we have documented in Section II, the refractive effect of the internal waves can cause artificial structures. In sidescan images, regular SAS images, and SAS bathymetry, these structures appear as one would expect a true topography feature to appear and are thus very difficult to differentiate from true topography. It is important to establish whether it is possible to detect or distinguish a water-column-induced feature from one that is actually a true seabed feature. In this section, we list candidate techniques for recognition of these features, and show example results.

The basic assumption we start with follows the study of the refractive effect in Section III. For these internal waves to create artificial features in the images, a few general conditions must be fulfilled.

- The ocean environmental conditions should be correct for the existence of internal waves and boluses that produce gradients of the correct shape (convex) in both density and sound speed.
- The sonar depth and orientation toward the seabed must allow for such features to be visible.
- The oceanographic features should move slowly.

When these three conditions are fulfilled, certain apparent structures ("ridges" and similar) in the sonar images can be created by refractive effects from these internal wave-related features. All three of these conditions were met during the Elba Island experiment in October 2012.

A. Repeat Pass Imaging and Interferometry

The refractive effect of the assumed internal wave boluses are clearly visible and detectable when running controlled repeated passes where the vehicle track is very similar in each pass. A noncoherent-image-based change detection technique
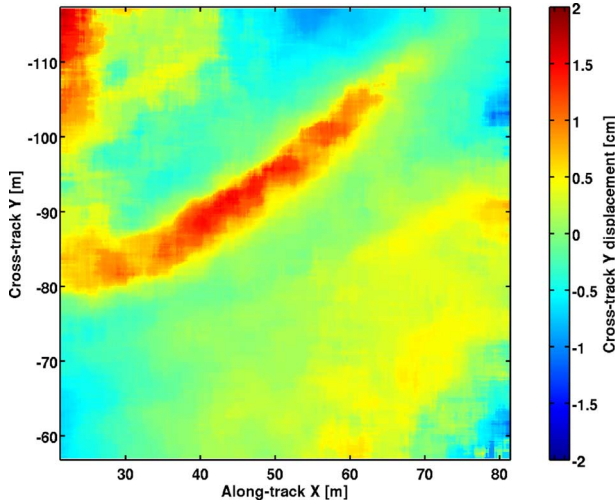
Fig. 11.   Repeat pass interferometry between the two images in Fig. 2. Estimated y-shift (cross-track) in centimeters. The color represents the interval $[-2, 2]$ cm for the displacement.
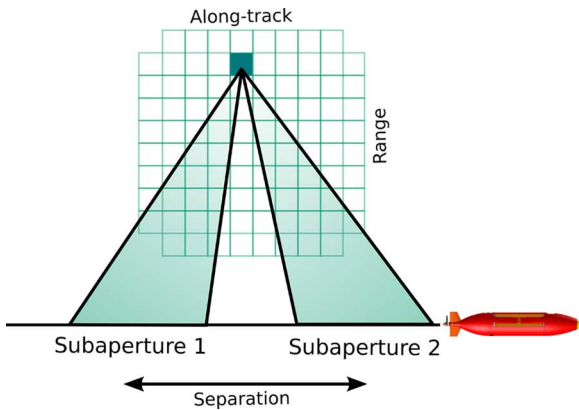

Fig. 12.   Principle of multiaperture SAS imaging.

[31] is sufficient for detection of the waves. Repeat pass imaging and mapping in a controlled fashion, where images of the same scene from the same look angle are made repeatedly with a suitable temporal baseline, would be ideal for detection, mapping, and characterization of the internal wave-related phenomena.

Repeat pass interferometry in SAR [25], [4, Ch. 4] uses images in repeated passes to estimate the topography as well as changes both in terrain and in the images. For stationary scenes and controlled data acquisition coherent change detection [22] may be applied, where changes not visible in the magnitude images can be detected. Note that the ocean environment may be a time-varying medium that changes the seabed such that there is a natural temporal decorrelation time for the seabed itself [32]. For sufficiently high repeat pass coherence, the apparent displacement of the backscattered signal (the speckle) for the signal that propagates through the water column feature can be estimated.

Following the technique described in [33], we have performed repeat pass interferometry processing on the two images shown in Fig. 2. Fig. 11 shows the estimated shift along the ground range axis (the y-axis). The results are median filtered to emphasize the effect of large scale motion. The average repeat pass coherence is 0.485 for these data. The results indicate a slowdown of the rays traveling through the assumed internal

wave bolus that displaces the backscattered signal behind the feature around 1.5 cm. This is, as expected, lower than the modeled shift in Section III.

B. Multiaperture With Temporal Separation

Often the data collection only contains a single image (or a single pass), so the techniques discussed in Section IV-A cannot be used. If only a single pass is available, an intuitive technique is to divide the total length of the synthetic aperture into subapertures with a certain temporal separation, as illustrated in Fig. 12. This is a well-known technique in the SAS field [34], [35], where the reason for doing this is to obtain images of different aspect angle on a potential target. In this particular case, we use a common imaging grid where nonoverlapping pings are used in each subaperture image [36].

There is a fundamental disadvantage of using this technique. A shorter synthetic aperture will lead to poorer along-track resolution. In the case of detection of moving internal wave features, the main parameter is the temporal baseline (or separation). The wave is expected to move on the order of 5–10 cm/s [27]. To use this technique, one must therefore choose a suitable temporal baseline which gives reasonable probability to detect the wave movement.

Fig. 13 shows two subaperture images of one of the suspected internal wave boluses at far range. The yellow lines are at fixed positions serving as guidelines for detection of wave movement. In this particular case, the temporal separation between the images is 21 s, and the integration time per image is 20.5 s. We see that the wave feature has moved between the temporal looks, although not clearly. A small investigation of this movement indicates that the wave phenomenon has moved approximately 65 cm (maximally), which equals an estimated wave speed of 3 cm/s. There is, however, a potential source for error in this analysis. Images from nonoverlapping temporal subapertures may have differences in the horizontal wave number coverage (see Section IV-C). This might lead to misinterpretation between wave movement and the refractive effects caused by the features as observed with different wave number coverages.

C. Multilook From Wave Number Filtering

A similar, although not identical, technique to the one proposed in Section IV-B is to divide the wave number spectrum into sections and form images from each of them [3, Ch. 3.8]. This is known in the SAR and SAS communities as multilook processing, as the properties of randomly distributed scatterers ensure that each look contains essentially the same scene [23, Ch. 3.3]. Multilooking is usually used as a means of reducing speckle. However, potential wave number dependence in the scene content (i.e., where the holographic property is not fulfilled [23, Ch. 3.3]) can be exploited to infer additional information. The most common example of this in spotlight-mode SAR is to divide the collection into subapertures to better observe moving target signatures and other changes happening on short time scales [37].

Interestingly, temporal and wave number subapertures are roughly equivalent for spotlight mode. However, there is a clear distinction between the domains for stripmap synthetic aperture
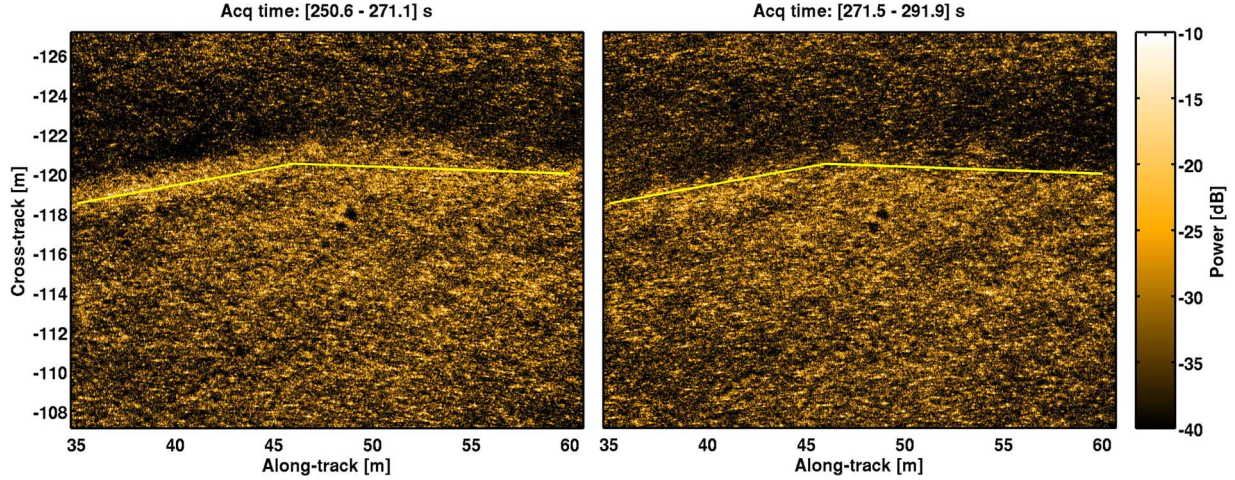
Fig. 13.   Multiaperture SAS images of the internal wave phenomenon. The yellow line is in fixed position in both images.
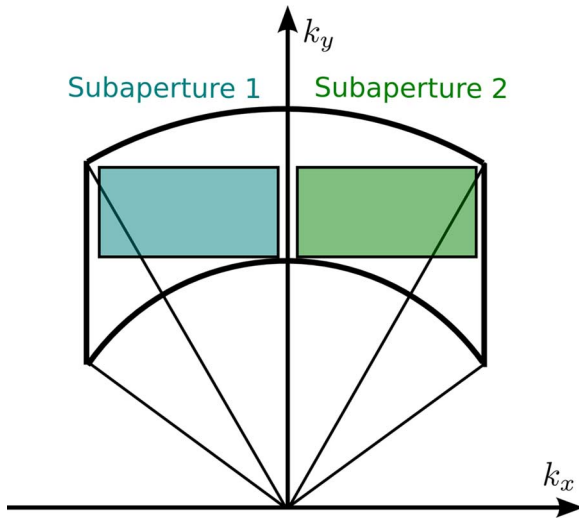

Fig. 14.   Principle of multilook from wave number filtering.

data collections [3, Ch. 1.3]. One may choose temporal subapertures as in Section IV-B or wave number subapertures. The latter can be thought of as angular filters. Consider the division shown in Fig. 14. The images resulting from these two subapertures would contain the same scene content and have the same interval of collection time. However, one image would correspond to a forward-looking beam, and the second to an aft-looking beam. Such imagery is useful for detecting internal waves only if there is a detectable change in refraction when the wave is viewed from different angles.

We might also multilook in the range wave number dimension. The resulting images will again possess identical content for areas obeying the holographic property. This time, however, effects that vary with frequency, rather than angle, will induce differences between the images. The implication for detecting internal waves is the subject of ongoing research. The ray model of propagation indicates that the acoustical path is effectively independent of frequency. However, the coherent interference of the rays is a function of frequency, and thus may offer a means of detecting internal waves.

It is conceivable that internal waves can cause differences between images created from spectral subapertures. The question

of determining the conditions under which these differences can be detected and measured remains to be answered. One difficulty is the fact that the subaperture images cannot be coherently compared because each contains an independent realization of the speckle. Detection must therefore rely on less sensitive approaches based on changes in image intensity. The variation between subapertures may be very slight, rendering the internal waves virtually undetectable using this method.

D. Backscatter and Topography Comparison

The refractive effect of an internal wave bolus will cause changes in the backscattered signal and the estimated seabed topography from interferometry (see Section III). A potential technique is then to compare the measured backscattered signal with a signal that would be backscattered from the estimated seabed topography. A misfit between the two can potentially be used to classify a feature as water column induced.

We have examined this technique on the suspected internal wave bolus shown in Fig. 2. We have calculated the expected backscattered difference from the estimated topography difference based on the interferometry estimates from the two passes. Perturbation theory [28, Ch. 13] was used to model the backscattered intensity. We can compare the estimated difference with the measured backscatter difference between the two passes. In this example, we have despeckled the results to emphasize the water column effect. The modeled and measured backscatter difference images are shown in Fig. 15. There are differences in the two images. Particularly, the modeled backscatter difference shows the wave patterns more clearly. This is due to lower variance in the estimated bathymetry compared to the estimated backscatter and thereby more easily detectable small changes (compare Fig. 3 with Fig. 5). Another noticeable difference is that the modeled highlight and shadow contrast is stronger than the measured one. This indicates leakage of acoustical signal into the shadow region (as also shown in Fig. 10). Whether these differences are substantial enough for reliable detection of water-column-induced features remains unclear. Note that there is a fundamental limitation to this technique: The seabed type has to be known within certain bounds, modeled with a sufficiently accurate model, and not change over the scene that
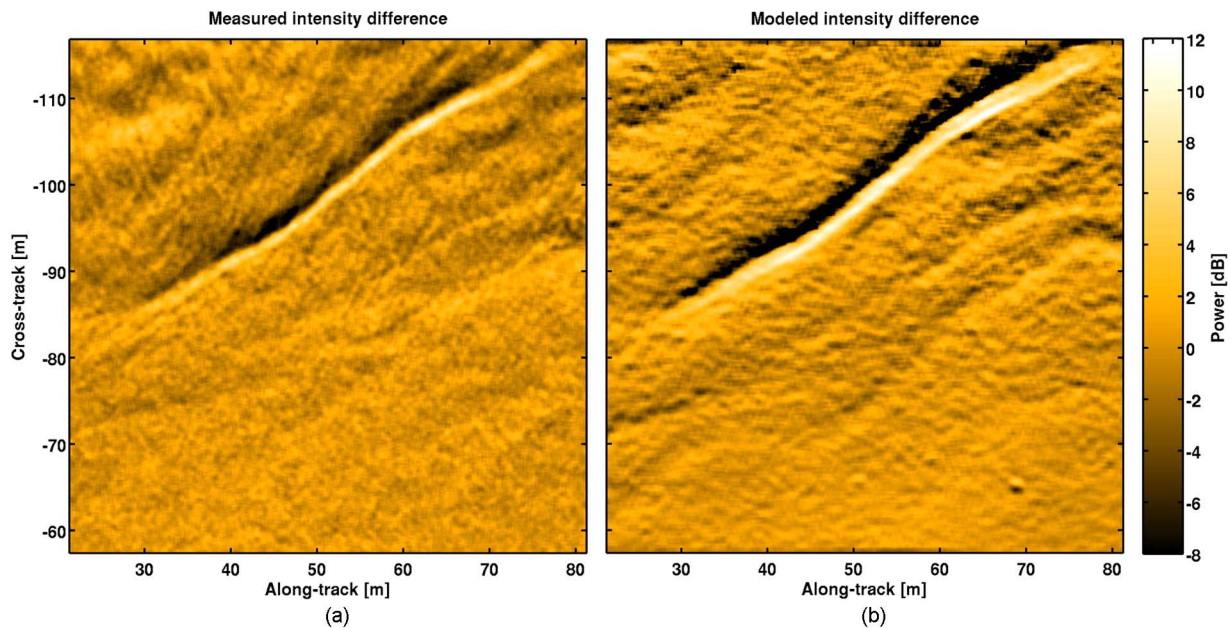
Fig. 15. (a) Measured intensity difference compared with (b) modeled intensity difference from topography and slope change.

is investigated. This is the same limitation one encounters in shape-from-shading-type processing [38].

E. Along-Track Interferometry

Repeat pass interferometry (see Section IV-A) is based on constructing interferograms representing phase and magnitude differences between coregistered images from repeated passes with a temporal separation (or baseline) that is suitable for studying the changes in the scene. One possibility is to use redundant transmitter/receiver elements to form two or more individual and coregistered synthetic aperture images from a single pass (multichannel synthetic apertures). This gives a very short temporal baseline (down to one pulse repetition) between the images. There are several approaches for detecting changes and moving objects in single-pass multichannel images: along-track interferometry (ATI) is based on forming interferograms between the images, and detecting changes in the phase differences [39, Ch. 7.3.2], [40] (similar to coherent change detection). Another approach is to subtract the images to suppress clutter (or unwanted signal), such that low signature changes can be more easily detected. This is known as displaced phase center antenna (DPCA) in SAR [41] (not to be confused with the DPCA technique reported in SAS [12] which is similar but used in another application). Both techniques have the potential to reduce the stationary signals such that a weakly moving target signature can be detected. Exactly which approach is preferred is dependent on the system, the geometry, and the application [42].

Most current SAS systems are multielement receiver systems due to the along-track sampling criterion [2]. To obtain two or more fully populated synthetic apertures for ATI, the number of overlapping phase centers must be more than half the number of receiver channels. This is a major limitation, and such data were not recorded during the ARISE'12 trials.

F. Moving Target Synthetic Aperture Imaging

Moving targets in general do not obey the criterion for synthetic aperture imaging unless their velocity and trajectory is compensated for correctly [43]. The effect of assuming that the scene is stationary under the synthetic aperture image formation is that a moving target will be displaced and smeared. This is documented well in SAR [39, Ch. 7], [44, Ch. 5.2]. One potential way to estimate the motion of a feature in a synthetic aperture image is to apply time–frequency analysis on the feature in the image [39, Ch. 7.3]. A moving target would induce a certain time–frequency relation that can be detected in certain cases. This is a technique that does not require multiple antennas, as the ATI/DPCA techniques do. Since the scene to be imaged (the seabed) is stationary, this technique will work poorly, and substantially worse than the ATI/DPCA techniques.

G. Doppler Estimation

The bolus phenomenon moves with a given speed. A potential technique is to estimate the speed directly from Doppler shift estimation (fast time) ideally on a single pulse echo. The internal wave itself does not cause any backscattered signal but affects the acoustical signals in two ways: a refractive ray bending effect that moves the intensity distribution (not the scatterers), and a decrease in the wave speed through the moving feature which causes displacement of the scatterers in the image. This means that there is very little (fast time) Doppler shift of the signal which requires a relative velocity between transmitter–scatterer–receiver.

H. Defocusing Effect

A weaker but potentially detectable effect is the fact that the bolus transports water of lower sound speed. The acoustical signal propagating through the waves will cause defocusing in the SAS images if not compensated for. However, the traveled distance through the water with incorrect sound speed is short — on the order of a few meters, which again leads to very mild
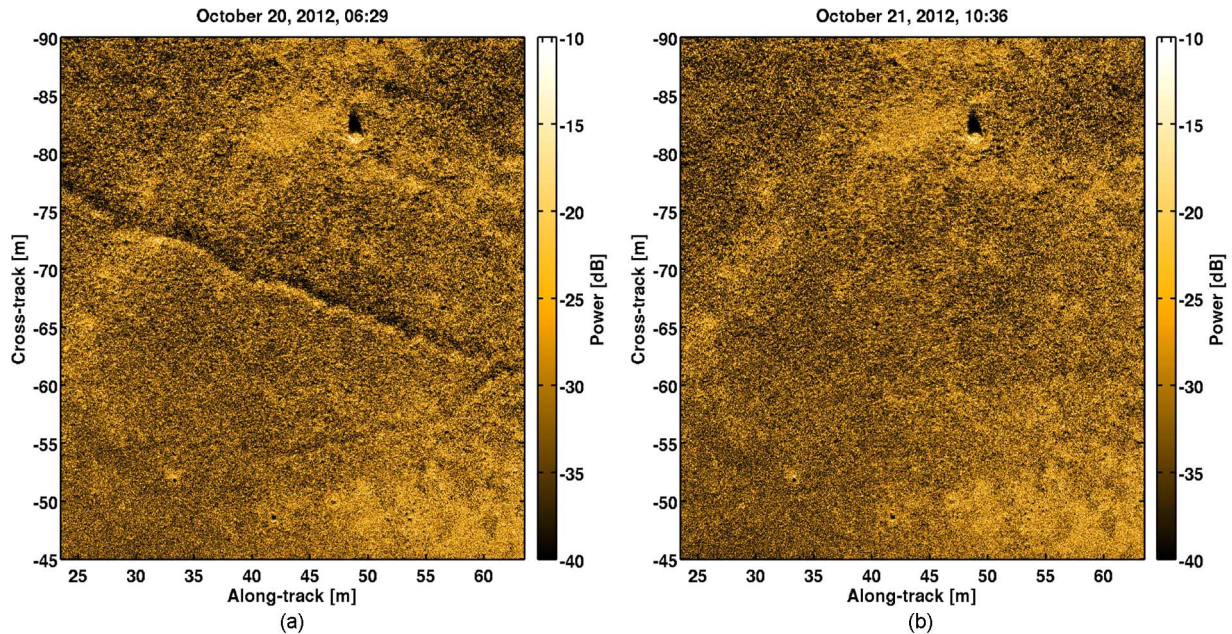
Fig. 16.   SAS image taken of the same scene 28 h apart. Panel (a) is the earliest. The apparent small ridge in the earliest SAS image is water column induced, and completely vanished in the last SAS image. The other objects and the seabed texture are preserved and do not change significantly between the two passes.

and maybe undetectable defocus. The primary effect of this will be the displacement described in Section III and not the defocus.

I. Summary of Techniques

In this section, we have listed some candidate techniques to detect and verify that a certain observable feature in a SAS image is caused by a water column effect. Based on a simple assessment of the techniques, our conclusions are as follows.

- The techniques described in Sections IV-E–IV-H will work poorly or not at all.
- The techniques described in Sections IV-B–IV-D have potential to work, but the detection will be difficult.
- The technique described in Section IV-A, which includes data collections in repeated passes, is preferred, and will provide sufficient data for accurate detection and potential characterization of the water column effects.

V. Conclusion

SAS is a tool well suited for detailed investigations of the seabed. As with all other types of sonar, SAS may be affected by the ocean environment and the sound-speed profile in particular. Internal waves are common in a layered ocean environment, possibly causing refractive effects for SAS. In this paper, we have presented SAS images from repeated passes of the same area, where strong features apparently on the seabed were not present 28 h later. To emphasize the effect of the phenomenon, we present a final data example in Fig. 16.

We have presented a simple geometrical theory that explains how a feature that results from a breaking internal wave (a bolus) can cause refractive effects that fit well with the observations. Hence, we believe the apparent strong features on the seabed are caused by a refracting water column effect. These features appear very similar to actual seabed topography in sidescan sonar images, SAS images, and SAS bathymetry. Such refractive effects from internal wave boluses can only occur

when a strong density and sound-speed step intersects a sloping seabed, and the sonar viewing geometry is advantageous.

We have presented different techniques to detect and distinguish these water column effects from real features on the seabed. The most favorable technique is to run repeated passes and perform noncoherent image-based change detection or differential interferometry. For cases when only single-pass data are available, we have presented two techniques that potentially might prove successful: multiaperture processing and multilook processing combined with displacement estimation. The phenomenon discussed in this paper moves very slowly, so that these techniques will require a relatively large temporal separation between looks.

For applications such as change detection, SAS is becoming a common tool. Operations in the littoral zone may be affected by ocean environmental variability. In such cases, it is important to distinguish between real features on the seabed and effects caused solely by the water column. In this paper, we have shown that the refractive effect of internal waves can cause strong features that resemble features on the seabed. Finally, the data presented in this paper strongly suggest that the state-of-the-art SAS, especially when collecting data in repeated passes, is sufficiently advanced to be used for detailed investigations of the oceanographic processes underlying the variations in water column properties.

REFERENCES

[1] M. P. Hayes and P. T. Gough, "Synthetic aperture sonar: A review of current status," *IEEE J. Ocean. Eng.*, vol. 34, no. 3, pp. 207–224, Jul. 2009.

[2] R. E. Hansen, "Introduction to synthetic aperture sonar," in *Sonar Systems*, N. Z. Kolev, Ed. Rijeka, Croatia: Intech, Sep. 2011, ch. 1, pp. 3–28 [Online]. Available: http://www.intechopen.com/books/sonar-systems

[3] G. Franceschetti and R. Lanari, *Synthetic Aperture Radar Processing*. Boca Raton, FL, USA: CRC Press, 1999.

[4] D. Massonnet and J. Souyris, *Imaging With Synthetic Aperture Radar*, ser. Engineering Sciences. Lausanne, Switzerland: EFPL Press, 2008.

[5] D. D. Sternlicht, T. G-Michael, and C. A. Matthews, "Advances in seabed change detection for port and coastal security," in *Proc. Int. Conf. Waterside Security*, May 2012.

[6] X. Lurton, *An Introduction to Underwater Acoustics: Principles and Applications*, 2nd ed. Chichester, U.K.: Springer–Praxis, 2010.

[7] H. J. Callow, T. O. Sæbø, S. A. Synnes, and R. E. Hansen, "SAS beamforming through a vertical sound speed profile," in *Proc. Underwater Acoust. Meas.*, Kos, Greece, Jun. 2011, pp. 561–568.

[8] R. E. Hansen, H. J. Callow, T. O. Sæbø, and S. A. V. Synnes, "Challenges in seafloor imaging and mapping with synthetic aperture sonar," *IEEE Trans. Geosci. Remote Sens.*, vol. 49, no. 10, pp. 3677–3687, Oct. 2011.

[9] F. S. Henyey *et al.*, "Effects of internal waves and turbulence on a horizontal aperture sonar," *IEEE J. Ocean. Eng.*, vol. 22, no. 2, pp. 270–280, Apr. 1997.

[10] J. T. Christoff, C. D. Loggins, and E. L. Pipkin, "Measurement of the temporal phase stability of the medium," *J. Acoust. Soc. Amer.*, vol. 71, no. 6, pp. 1606–1607, Jun. 1982.

[11] P. T. Gough and M. P. Hayes, "Measurements of acoustic phase stability in Loch Linnhe, Scotland," *J. Acoust. Soc. Amer.*, vol. 86, no. 2, pp. 837–839, Aug. 1989.

[12] A. Bellettini and M. A. Pinto, "Theoretical accuracy of synthetic aperture sonar micronavigation using a displaced phase-center antenna," *IEEE J. Ocean. Eng.*, vol. 27, no. 4, pp. 780–789, Oct. 2002.

[13] M. A. Pinto, "High resolution seafloor imaging with synthetic aperture sonar," *IEEE Ocean. Eng. Newslett.*, pp. 15–20, 2002.

[14] K. R. Helfrich, "Internal solitary wave breaking and run-up on a uniform slope," *J. Fluid Mech.*, vol. 243, pp. 133–154, Oct. 1992.

[15] B. C. Wallace and D. L. Wilkinson, "Run-up of internal waves on a gentle slope in a two-layered system," *J. Fluid Mech.*, vol. 191, pp. 419–442, Jun. 1988.

[16] S. K. Venayagamoorthy and O. B. Fringer, "On the formation and propagation of nonlinear internal bolusess across a shelf break," *J. Fluid Mech.*, vol. 577, pp. 137–159, Apr. 2007.

[17] D. Bourgault, M. D. Blokhina, R. Mirshak, and D. E. Kelley, "Evolution of a shoaling internal solitary wave train," *Geophys. Res. Lett.*, vol. 34, no. 3, Feb. 2007, DOI: 10.1029/2006GL028462.

[18] F. M. Dickey, J. M. DeLaurentis, and A. W. Doerry, "A SAR imaging model for large-scale atmospheric inhomogeneities," *Proc. SPIE—Int. Soc. Opt. Eng.*, vol. 5410, pp. 1–9, Aug. 2004.

[19] A. Muschinski, F. M. Dickey, and A. W. Doerry, "Possible effects of clear-air refractive-index perturbations on SAR images," *Proc. SPIE—Int. Soc. Opt. Eng.*, vol. 5788, pp. 25–33, Mar. 2005.

[20] F. M. Dickey, A. W. Doerry, and L. A. Romero, "Degrading effects of the lower atmosphere on long range SAR imaging," *IET Radar Sonar Navig.*, vol. 1, no. 5, pp. 329–339, Oct. 2007.

[21] P. E. Hagen, T. G. Fossum, and R. E. Hansen, "HISAS 1030: the next generation mine hunting sonar for AUVs," in *Proc. UDT Pacific Conf.*, Sydney, N.S.W., Australia, Nov. 2008.

[22] M. Preiss and N. J. S. Stacy, "Coherent change detection: Theoretical description and experimental results," Defence Science and Technology (DSTO), Australia, Tech. Rep. DSTO-TR-1851, 2006.

[23] J. C. V. Jakowatz, D. E. Wahl, P. H. Eichel, D. C. Ghiglia, and P. A. Thompson, *Spotlight-Mode Synthetic Aperture Radar: A Signal Processing Approach*. Dordrecht, The Netherlands: Kluwer, 1996.

[24] T. O. Sæbø, S. A. V. Synnes, and R. E. Hansen, "Wideband interferometry in synthetic aperture sonar," *IEEE Trans. Geosci. Remote Sens.*, vol. 51, no. 8, pp. 4450–4459, Aug. 2013.

[25] R. F. Hanssen, *Radar interferometry: Data interpretation and error analysis*. Dordrecht, The Netherlands: Kluwer, 2001.

[26] L. Brekhovskikh and Y. Lysanov, *Fundamentals of Ocean Acoustics*, ser. Electrophysics. Berlin, Germany: Springer-Verlag, 1982, vol. 8.

[27] A. P. Lyons, R. E. Hansen, T. O. Sæbø, and H. J. Callow, "Refractive effects of internal waves on synthetic aperture sonar images," in *Proc. 1st Underwater Acoust. Conf.*, Corfu, Greece, Jun. 2013, pp. 93–101.

[28] D. Jackson and M. Richardson, *High-Frequency Seafloor Acoustics*. New York, NY, USA: Springer-Verlag, 2007.

[29] Applied Physics Laboratory, University of Washington, "High-frequency ocean environment acoustic models handbook," Seattle, WA, USA, Tech. Rep. APL-UW TR 9407, Oct. 1994.

[30] T. O. Sæbø, "Seafloor depth estimation by means of interferometric synthetic aperture sonar," Ph.D. dissertation, Dept. Phys. Technol., Univ. Tromsø, Tromsø, Norway, 2010.

[31] Ø. Midtgaard *et al.*, "Change detection using synthetic aperture sonar: Preliminary results from the Larvik trial," in *Proc. MTS/IEEE OCEANS Conf.*, Kona, HI, USA, Sep. 2011.

[32] A. P. Lyons and D. C. Brown, "The impact of the temporal variability of seafloor roughness on synthetic aperture sonar repeat-pass interferometry," *IEEE J. Ocean. Eng.*, vol. 38, no. 1, pp. 91–97, Jan. 2013.

[33] T. O. Sæbø, R. E. Hansen, H. J. Callow, and S. A. Synnes, "Coregistration of synthetic aperture sonar images from repeated passes," in *Proc. Underwater Acoust. Meas.*, Kos, Greece, Jun. 2011, pp. 529–536.

[34] J. E. Fernandez and J. T. Christoff, "Multi-aspect synthetic aperture sonar," in *Proc. MTS/IEEE OCEANS Conf.*, Providence, RI, USA, Sep. 2000, pp. 177–180.

[35] D. A. Cook, J. T. Christoff, and J. E. Fernandez, "Broadbeam multiaspect synthetic aperture sonar," in *Proc. MTS/IEEE OCEANS Conf.*, Honolulu, HI, USA, Nov. 2001, pp. 188–192.

[36] R. E. Hansen, H. J. Callow, T. O. Sæbø, P. E. Hagen, and B. Langli, "High fidelity synthetic aperture sonar products for target analysis," in *Proc. OCEANS Conf.*, Quebec, QC, Canada, Sep. 2008, DOI: 10.1109/OCEANS.2008.5152071.

[37] K. Ouchi, "On the multilook images of moving targets by synthetic aperture radars," *IEEE Trans. Antennas Propag.*, vol. AP-33, no. 8, pp. 823–827, Aug. 1985.

[38] E. Coiras, Y. Petillot, and D. M. Lane, "Multiresolution 3-D reconstruction from side-scan sonar images," *IEEE Trans. Image Process.*, vol. 16, no. 2, pp. 382–390, Feb. 2007.

[39] V. C. Chen and H. Ling, *Time-Frequency Transforms for Radar Imaging and Signal Analysis*. Boston, MA, USA: Artech House, 2002.

[40] P. A. Rosen *et al.*, "Synthetic aperture radar interferometry," *Proc. IEEE*, vol. 88, no. 3, pp. 333–382, Mar. 2000.

[41] C. E. Muehe and M. Labitt, "Displaced-phase-center antenna technique," *Lincoln Lab. J.*, vol. 12, no. 2, pp. 281–296, 2000.

[42] S. Chiu and C. Livingstone, "A comparison of displaced phase centre antenna and along-track interferometry techniques for RADARSAT-2 ground moving target indication," *Can. J. Remote Sens.*, vol. 31, no. 1, pp. 37–51, Feb. 2005.

[43] R. K. Raney, "Synthetic aperture radar (SAR) images of moving targets," *IEEE Trans. Aerosp. Electron. Syst.*, vol. AES-7, no. 3, pp. 499–505, May 1971.

[44] M. Soumekh, *Fourier array imaging*. Englewood Cliffs, NJ, USA: Prentice-Hall, 1994.

Roy Edgar Hansen (M'07) received the M.Sc. and Ph.D. degrees in physics from the University of Tromsø, Tromsø, Norway, in 1992 and 1999, respectively.

From 1992 to 2000, he was with the Norwegian research company TRIAD, working on multistatic sonar, multistatic radar, synthetic aperture radar (SAR), and underwater communications. Since 2000, he has been with the Norwegian Defence Research Establishment (FFI), Kjeller, Norway. He is currently Principal Scientist and team leader for the autonomous underwater vehicle development and the synthetic aperture sonar development at FFI. He is also Adjunct Associated Professor at the Centre for Imaging, University of Oslo, Oslo, Norway.

Anthony P. Lyons (M'96) received the B.S. degree (*summa cum laude*) in physics from the Henderson State University, Arkadelphia, AR, USA, in 1988 and the M.S. and Ph.D. degrees in oceanography from Texas A&M University, College Station, TX, USA, in 1991 and 1995, respectively.

He was a Scientist at the SACLANT Undersea Research Centre, La Spezia, Italy, from 1995 to 2000, where he was involved in a variety of projects in the area of environmental acoustics. Currently, he is a Senior Scientist at the Applied Research Laboratory, Pennsylvania State University (ARL–PSU), University Park, PA, USA, where he is engaged in studies of high-frequency acoustical interaction with the seafloor and sea surface.

Dr. Lyons was awarded, with the recommendation of the Acoustical Society of America, the Institute of Acoustics (U.K.) A.B. Wood Medal "for distinguished contributions in the underwater application of acoustics" in 2003. He is a Fellow of the Acoustical Society of America and a member of the IEEE Oceanic Engineering Society.

Torstein Olsmo Sæbø (M'06–SM'13) was born in Bergen, Norway, in 1977. He received the cand.scient (M.Sc.) degree in astrophysics from the University of Oslo, Oslo, Norway, in 2002 and the Ph.D. degree in physics from the University of Tromsø, Tromsø, Norway, in 2010, with a dissertation entitled "Seafloor depth estimation by means of interferometric synthetic aperture sonar.

Since 2002, he has been with the Norwegian Defence Research Establishment (FFI), Kjeller, Norway, specializing in the field of interferometry on synthetic aperture sonar. He is currently a Senior Scientist at FFI.

Dr. Sæbø is a newly appointed Associate Editor for the IEEE JOURNAL OF OCEANIC ENGINEERING.

Hayden John Callow (M'07) received the B.E. degree in electrical and electronic engineering from the University of Canterbury, Christchurch, New Zealand, in 1998 and the Ph.D. degree in synthetic aperture sonar (SAS) image enhancement from the Acoustics Research Group, University of Canterbury, in 2003.

He joined the Norwegian Defence Research Establishment (FFI), Kjeller, Norway, in 2004, where he worked within the autonomous underwater vehicle (AUV) research team on synthetic aperture sonar (SAS) imaging sensors, primarily performing research into SAS beamforming, micronavigation, and interferometry. In 2011, he joined Kongsberg Maritime, Horten, Norway, where he works as an SAS R&D Engineer.

Daniel A. Cook (M'07–SM'08) received the B.S. and M.S. degrees in mechanical engineering and the M.S. degree in electrical and computer engineering from the Georgia Institute of Technology, Atlanta, GA, USA, in 1998, 2000, and 2007, respectively.

From 2000 to 2007, he was with the Naval Surface Warfare Center, Panama City, FL, USA, where he developed techniques for synthetic aperture sonar (SAS) motion estimation and compensation. Currently, he is with the Sensors and Electromagnetic Applications Laboratory, Georgia Tech Research Institute (GTRI/SEAL), Atlanta, GA, USA, where his research is in the area of synthetic aperture radar (SAR) imaging and adaptive radar signal processing.